Controlled Interfacial Reactions and Superior Mechanical Properties of High Energy Ball Milled/Spark Plasma Sintered Ti-6Al-4V-Graphene Composite

Y. Zhou [a], L.L. Dong [b, c, *], Q.H. Yang [a, *], W.T. Huo [b], Y.Q. Fu [d], Y.J. Shi [c], Y. Liu [b], Y.S. Zhang [e]

[a] School of Materials Science and Engineering, Xi'an University of Science and Technology, Shaanxi, Xi'an 710054, PR China

[b] Advanced Materials Research Central, Northwest Institute for Nonferrous Metal Research, Xi'an 710016, PR China

[c] School of Materials Science and Engineering, Northeastern University, Shenyang 110819, PR China

[d] Faculty of Engineering and Environment, Northumbria University, Newcastle upon Tyne NE1 8ST, UK

[e] Xi'an Rare Metal Materials Institute Co., Ltd, Xi'an, 710016, PR China

Abstract:

Ball milling process has become one of the effective methods for dispersing graphene nanoplates (GNPs) uniformly into a metal matrix, however, there are often serious issues of structural integrity and interfacial reactions of these GNPs with the

* Corresponding author:
E-mail: donglong1027@163.com (L.L. Dong), yangxjtu@hotmail.com (Q.H. Yang)

matrix. In this work, we synthesized Ti-6Al-4V (TC4) matrix composites reinforced with GNPs using combined methods of high energy ball milling (HEBM) and spark plasma sintering (SPS). Effects of ball milling on evolution of microstructures and interfacial reactions of GNPs/TC4 composite powders during the HEBM were thoroughly investigated. When the ball milling time was increased up to 15 hrs, the average size of TC4 powders was firstly increased (e.g., ~104.15 μm, 5 hrs) due to severely plastic deformation, but then decreased to ~ 1.5 μm (15 hrs), which was much smaller than that of the original TC4 powders (~ 86.8 μm). TiC interfacial structures were *in-situ* formed on the surfaces of the TC4 particles when the ball milling time was 10 hrs. After SPS process using the composite powders, the GNPs/TC4 composites exhibited 36-103% increase in compressive yield strength and 57-78% increase in hardness than those of the TC4 alloy, whereas the fracture to strain was reduced nonlinearity (from 28% to 7%) with the increase of ball milling time (from 2 hrs to 15 hrs). A good balance between high strength (1.9 GPa) and ductility (17%) of the GNPs/TC4 composites was achieved when the ball milling time was 10 hrs, which can be attributed to the synergistic effects of grain refinement strengthening, solid solution strengthening, load transfer strengthening from the GNPs and *in-situ* formed TiC.

Keywords: Ball milling, Interfacial reaction, Spark plasma sintering, Mechanical properties

1. Introduction

Titanium matrix composites (TiMCs) are promising materials used for aerospace, petrochemical engineering and automobile industries owing to their excellent strength, low density, outstanding corrosion and abrasive resistance [1-3]. High performance TiMCs can be fabricated using powder metallurgy processes via introduction of reinforcements such as TiC, SiC, TiB, $(TiHf)_5Si_3$, carbon nanotubes (CNTs) [4-8] etc. Although these conventional reinforcements can improve the mechanical properties of TiMCs, it is generally difficult to achieve a good trade-off between strength and ductility.

The discovery of graphene in 2004 provides a new revenue for development of high-performance metal matrix composites (MMCs). Graphene and its derivatives have attracted great attention for synergistically improving the performance of light-weight matrix owing to their distinct 2D structures and extraordinary mechanical properties [9-12]. Previously Dong et al. [11] dispersed 0.3 wt.% graphene oxides nanosheets (GONs) into pure Ti powders using a hydrothermal synthesis method and sintered GONs/Ti composites via spark plasma sintering (SPS). Their results indicated that tensile strength of the sintered TiMC was increased by 9.7%, compared to that of sintered pure Ti matrix. However, the mechanical properties of Ti based MMCs often could not be further improved even when the graphene content has been significantly increased. Zhang et al. [13] achieved various graphene contents (0.25, 0.5, 0.75, 1 and 1.5 wt%) adsorbed onto the surfaces of polyvinyl alcohol-modified TC4 powders using a magnetic stirring method and then fabricated graphene/TC4 composites using

SPS. Their results showed that 0.25 wt% graphene/TC4 composites possessed the maximum tensile strength with a maximum elongation ratio of 10%. The main issue is the difficulties in achieving a homogeneous dispersion of graphene or its derivatives into the Ti matrix. Various dispersion methods, including flake powder metallurgy [14], high energy ball milling (HEBM) [15], metal nanoparticles modified graphene [16] and hydrothermal synthesis-assisted ball milling [17] have been applied. Among these methods, HEBM is one of the most economic and effective dispersion technologies for engineering applications. It has been successfully used to disperse graphene or its derivatives into metal matrix (Cu, Al etc.). For example, Chu et al [18] used a modified ball-milling process to obtain the uniform dispersion of reduced GONs onto the surfaces of the CuCr powders and then synthesized 2.5 vol% rGON/CuCr composites using SPS. These composites exhibited a tensile strength of 352 MPa, which is 82% higher than that of unreinforced CuCr alloy. An excellent balance of strength (295 MPa) and ductility (13.5%) of Al matrix composites was also achieved by vacuum sintering and hot extrusion of shift-speed ball milled GNPs/Al powders [19]. Recently, Mu et al investigated the size effects of the Ti powders on the mechanical properties of GNPs/Ti matrix composites using both HEBM and SPS. They found that the formed TiC nanoparticles/nanolayers during the sintering provide an effective load transfer capability for composites, thus improving their strength and ductility [20].

Generally, there are three predominant stages during the HEBM processes, e.g., plastic deformation, cold welding and fracture of the reinforcements and matrix powders [21]. Unlike copper and its alloys powders, due to the difficulties to severely

deform Ti alloys powders, there are few reports on refining their particle sizes by HEBM. Long et al. [22] utilized HEBM and SPS to prepare ultrafine-grained TC4 alloys, and obtained microstructures of TC4 matrixes with an average grain sizes of 0.51~0.89 mm. However, they only investigated the effect of ball milling times for the raw powders. In fact, Ti and its alloy powders will easily react with carbon atoms to formed non-stoichiometric titanium carbides during the HEBM processes, which will affect the GNPs' microstructures and the performance of the resulted composites.

Therefore, we focus the present work on the structural evolution and interfacial reactions of the GNPs and TC4 powders during the ball milling, and then study the mechanical properties and failure mechanisms of the synthesized TiMCs using these powders. For simplify, the as-sintered composites with different ball milling times of 0, 2, 5, 10 and 15 hrs were named as C0, C2, C5, C10 and C15, respectively. We found that the *in-situ* TiC phases were formed and embeded into the TC4 powders when the ball milling time is longer than 10 hrs, and therefore, a good balance between the strength (1.9 GPa) and ductility (17%) of the GNPs/TC4 composites can be well achieved.

2. Results and Discussion

2.1 Microstructural evolution of GNPs/TC4 powders in HEBM

Figure 1 shows scanning electron microscope (SEM) images of the GNPs/TC4 powders processed with different ball milling times. After 2 hrs ball milling, the powders shown in **Figure 1a** has almost a spherical shape with an average size of ~

89.64 μm. However, when the ball milling time is increased to 5 hrs, the average TC4 particle size is increased to 104.15 μm, with some flake morphologies as shown in **Figure 1b**. Only a few amounts of GNPs are dispersed and adhered on the surfaces of TC4 powders after 2h ball milling (**Figure 1a$_1$**). Nevertheless, a lot of GNPs are distributed on the surfaces of TC4 powders when the ball milling is 5 hrs (**Figure 1b$_1$**). With the ball milling time is increased to 10 hrs, spherical and flaky-shaped TC4 powder flakes are found to disappear in **Figure 1c** owing to the shear-crush mechanism induced by milling balls [23]. Furthermore, it was very difficult to locate the GNPs, which indicates that the majorities of the GNPs are embedded into the TC4 particles during the ball milling process. When the ball milling time is further prolonged to 15 hrs, the TC4 particles exhibit irregular particulate shapes with an average size of 1.50 μm, which is 98.6% reduction compared with the original powders (~86 um, **Figure 9d**). Based on SEM images in **Figures 1d and d$_1$**, the nano-scale TiC phases are covered on the surface of the TC4 powders without obvious GNPs. The presence of GNPs and TiC on the surface of TC4 powders provides a pinning effect and prohibits significant grain growth during the sintering.

The interfacial microstructures of the ball-milled GNPs/TC4 powders were further characterized using transmission electron microscope (TEM) and high-resolution TEM (HRTEM). Except a small number of agglomerated GNPs, tiny GNPs can be observed after 2 hrs ball milling (**Figure 2a),** which is attributed to that the shear force introduced by milling balls can exfoliate graphene nanolayers. In fact, previous studies showed that the appropriate ball milling parameters are in favor of

the graphene exfoliation from graphite [24]. The HRTEM image in **Figure 2b** shows that the interlayer space of GNPs is ~ 0.34 nm, which is consistent with the results reported in a previous study [9]. However, as the ball milling time was increased to 15 hrs, the layered structure morphology of GNPs was severely destroyed, and these GNPs were found to embed inside the TC4 particles (**Figure 2c**). The image in **Figure 2d** shows that lattice fringe of marginal GNPs is twisted and indistinctive, revealing that amorphous carbon are formed at the edges of these GNPs. Furthermore, some nanoscale white particles are found to embed inside TC4 particles (**Figure 2e**), which can be identified as TiC nanoparticles according to EDS analysis shown in **Figure 2f**.

Previous studies of Cu matrix composites using reduced graphene oxide (rGO) and CNTs as the carbon sources have shown that interfacial carbides are preferentially formed at the defective sites of the rGO and CNTs, because of the highly reactive nature of carbon atoms in these defects (pristine and produced) regions, as well as easy formation of carbides [25-28]. Therefore, the defect structures and distribution of carbon sources play critical roles in the nucleation and growth of these carbides. **Figure 2g** schematically summarizes the mechanisms for interfacial TiC phase formation and evolution of GNPs during the ball milling process. The large size of GNPs with some nanoscale defects (**Figure 9b**) are exfoliated and then crushed into small sizes under the shearing force of milling balls after short ball milling (i.e. 2 hrs and 5 hrs, **Figures 2a and b**), resulting in newly generated defects at the fracture edge of GNPs. For longer milling durations (such as 15 hrs), the average size of milled

TC4 powders (~1.5 um) was smaller than that with milling time of 2 hrs. In fact, the fine grain/ultra-fine grain Ti particles possess high activity and large specific surface area [29, 30]. When the mixed composite powders are subjected to long time ball milling process, some Ti atoms and carbon atoms are inter-diffused, and Ti atoms are quickly diffused to the highly reactive and amorphous carbon defects region, and then react with active carbon atoms of defects region to form TiC particles (**Figures 2e and f**). Furthermore, the HEBM is a non-equilibrium process of material preparation technology [31]. The chemical reactions can be induced at lower temperature or room temperature owing to the activation of the powders by mechanical energy. The long-time ball milling can result in increases of temperature and concentration of defects, which increase the reaction kinetics of *in-situ* formed TiC phase.

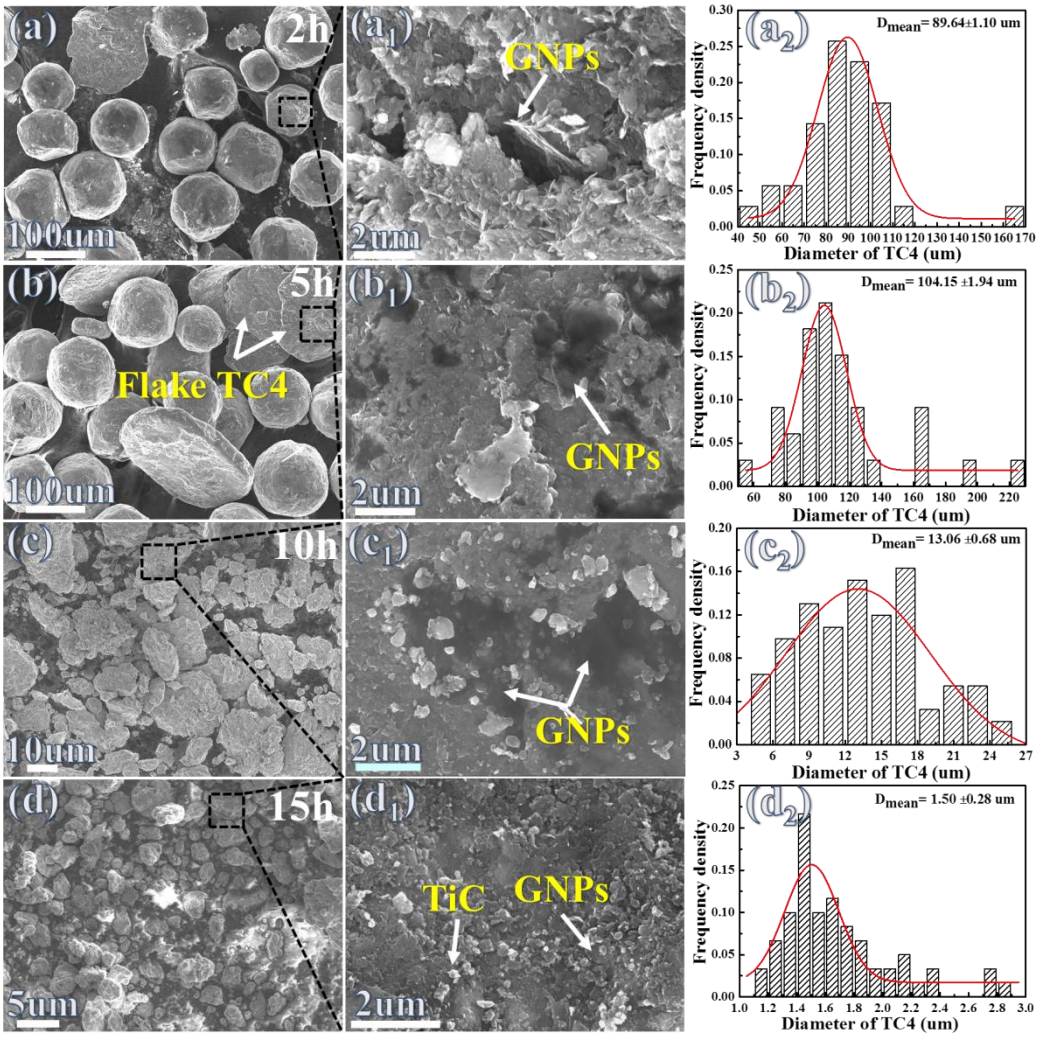

Figure 1. SEM morphologies and corresponding particle size distribution of TC4 with various balling times (a, a_1, a_2) 2 hrs, (b, b_1, b_2) 5 hrs, (c, c_1, c_2) 10 hrs, and (d, d_1, d_2) 15 hrs, respectively.

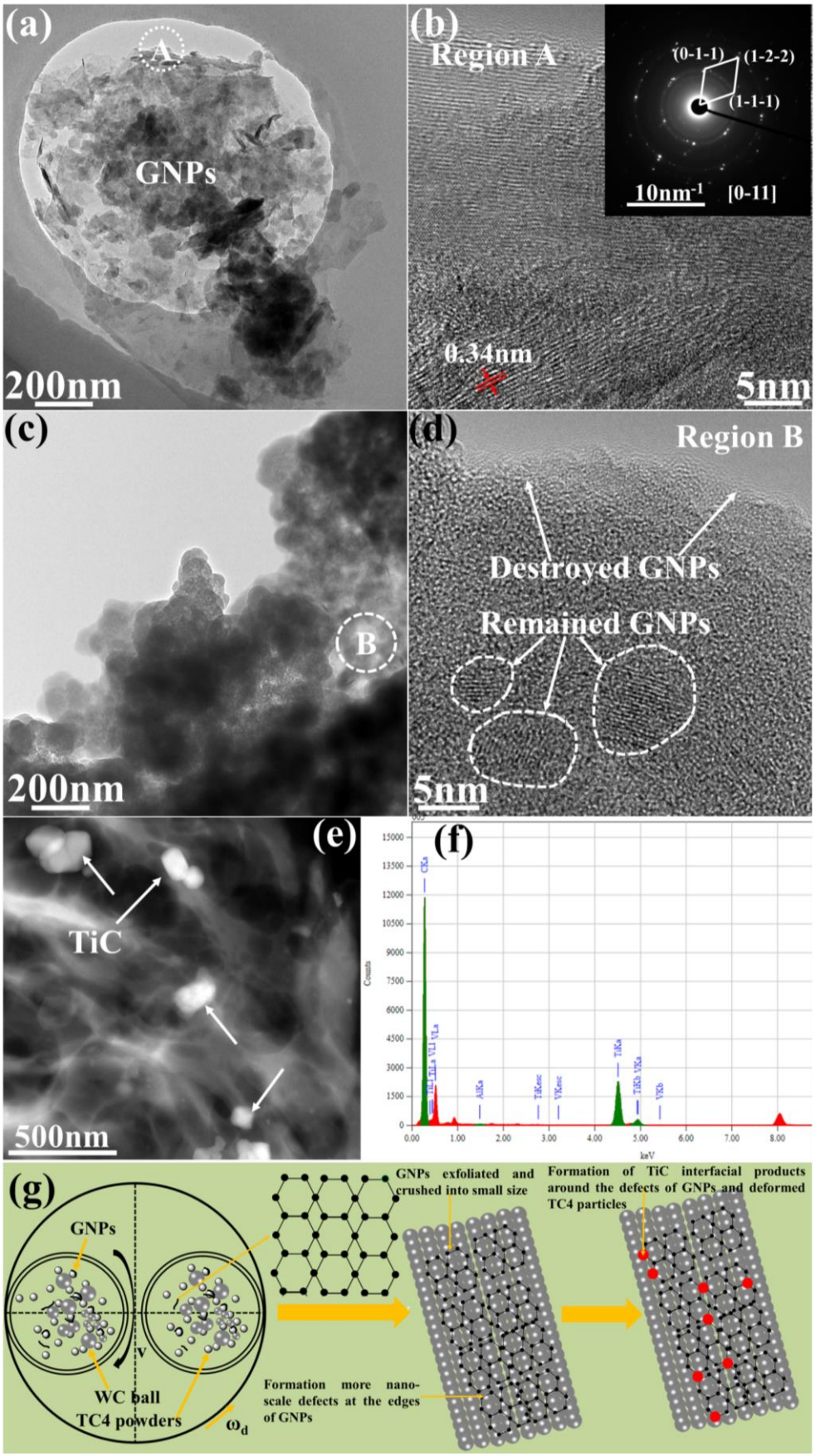

Figure 2. (a) TEM image of GNPs/TC4 mixture after 2 hrs ball milling, (b) HRTEM

image of remarked region A in (a) and inset is selected area diffraction pattern results of the region A; (c) TEM image of GNPs/TC4 mixture after 15 hrs ball milling, (d) HRTEM image of remarked region B in (c), (e) High-angle annular dark-field-scanning transmission electron microscope (HADDF-TEM) image of the interfacial products TiC inside in GNPs and (f) corresponding EDS point of TiC nanoparticles in (e); (g) The schematic diagram of interfacial products TiC formation and evolution of GNPs during the ball milling process, respectively.

2.2 Phase and composition of GNPs/TC4 powders in HEBM

Figure 3a shows X-ray diffraction (XRD) patterns of the milled GNPs/TC4 powders with various ball milling times. The main peaks corresponding to α-Ti are observed in the raw TC4 powders. However, peak broadening and density weakening can be observed with an increasing of ball milling times as shown in **Figure 3a**, revealing that the TC4 particles size is drastically reduced. The decrease in intensity of α-Ti in the milled powders can be linked to the formation of the interfacial products during the ball milling [30]. After 15 hrs milling, **Figure 3a** shows a new peak located at ~ 38.6°, which is attributed to that of TiC (200) (PDF# 02-4902). No GNPs are detected in the composite powders. This could be a result of the homogeneous dispersion of the GNPs in the surfaces of TC4 powders (**Figure 1**) and the amorphization of the GNPs during the ball milling [32].

The structures and nanoscale defects of GNPs in the milled composite powders were further characterized using Raman spectroscopy and the results are shown in

Figures 3b~c. There are three obvious characteristic peaks of the GNPs, i.e., D band (~1340 cm^{-1}, the defect band), G band (~1580 cm^{-1}) and 2D band (~2 700 cm^{-1}), as listed in **Table 1**. A progressive broadening of the D and G bands are observed with the increase of ball milling time for the composite powders. However, as the G band corresponds to the degree of graphitic arrangement and crystallinity of the C-atoms in the graphitic network of the GNPs, any broadening of this Raman peak is an indication of the presence of induced disorders or loss of crystallinity. Thus, our results show that the defect concentrations and crystallinity are decreased, and amorphization occurs with the increased ball milling time.

In **Figure 3b** there are additional Raman peaks located at ~ 418 cm^{-1} and ~ 605 cm^{-1} corresponding to the TiC phase, after milling for 10 hrs and 15 hrs,. The intensity ratio (I_D/I_G) of the D and G band is often used to evaluate the defects and quality of the carbon materials [9]. The I_D/I_G ratio is increased from 0.26 to 0.56 after 2 hrs milling and further increased to 1.52 when milling duration is 10 hrs (**Figure 3c**), revealing that the GNPs was severely destroyed, resulting in their amorphization.

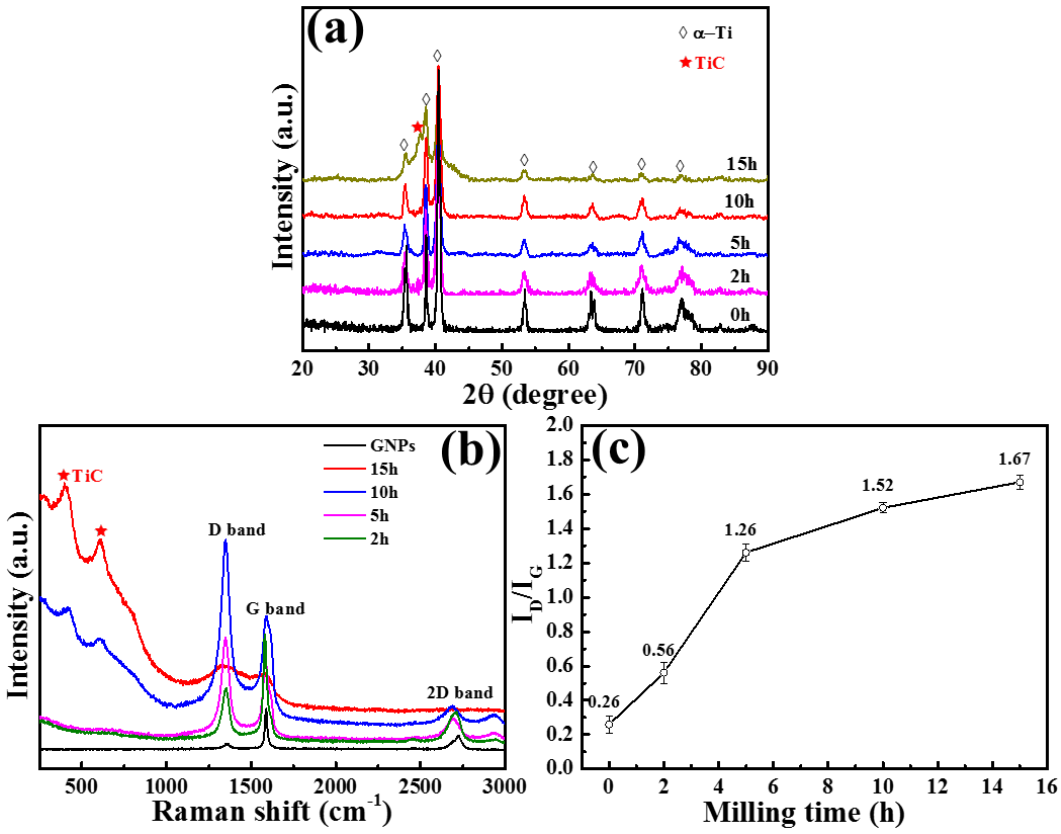

Figure 3. (a) XRD patterns, (b) Raman spectra of ball milled GNPs/TC4 mixtures, and (c) corresponding I_D/I_G results with an increasing of milling times, respectively.

Table 1. The detailed Raman spectra results of the ball milled composites powders.

Ball milling time	D band	G band	2D band	I_D/I_G
GNPs	1362.69	1586.29	2723.45	0.26
2h	1350.62	1582.31	2702.70	0.56
5h	1347.44	1583.86	2693.27	1.26
10h	1350.62	1590.03	2682.48	1.52
15h	1331.54	1577.68	2677.08	1.67

Figure 4 shows analysis results using high-resolution X-ray photoelectron spectroscopy (XPS), which can reveal the bonding characteristics of ball milled GNPs/TC4 mixture powders after various ball milling times. The C1s peak of raw

GNPs in **Figure 4a** reveals three main components arising from C=C sp^2, C-C sp^3 and C-O, located at ~ 284.8 eV, ~285.6 eV and ~286.4 eV, respectively [33]. As shown in **Figure 4a**, the intensity of sp^2 is much higher than that of sp^3 (sp^2/sp^3 ratio = 12.5), revealing that the raw GNPs shows a high degree of graphitization and low contents of nano-scale defects. With increase of the ball milling time, the ratio of the intensity (I_{sp2}/I_{total} and I_{sp3}/I_{total}) varies differently. Based on **Figures 4a~f**, the I_{sp3}/I_{total} ratio is gradually increased to 0.29 from a minimized value. Simultaneously, the I_{sp2}/I_{total} ratio decreases ~35% from 0.88 to 0.57 after 15 hrs ball milling process, which is linked with the increment of nano-scale defects in the GNPs. The low intensity peak at 282.3 eV which corresponds to the C-Ti bonds [34] appears in **Figure 4d** and reaches its maximum intensity of 0.09 after 15 hrs ball milling. XPS results clearly show that with the increase of ball milling time, GNPs have more nano-scale defects and easily react with Ti atoms to generate higher contents of TiC particles.

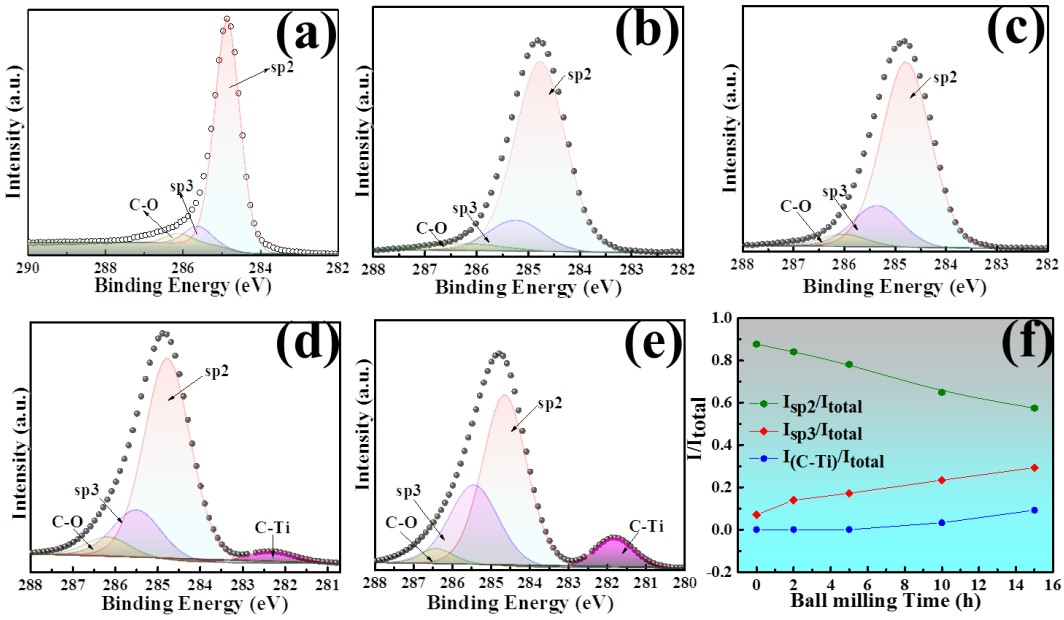

Figure 4. The C1s XPS spectra of the GNPs/TC4 composites powders after various times (a) 0 hrs, (b) 2 hrs, (c) 5 hrs, (d) 10 hrs, (e) 15 hrs, and (f) Evolution tendency of

structural integrity (I_{sp2}/I_{total}), The content of sp^3 C-C (I_{sp3}/I_{total}) and the extent of interfacial reaction ($I_{C\text{-}Ti}/I_{total}$) of the milled powders, respectively.

2.3 Microstructure and mechanical properties of GNPs/TC4 composites

The SEM images of sintered GNPs/TC4 with various ball milling times are shown in **Figure 5**. **Figure 5a** shows the typical Widmanstätten lamellar microstructure consisting of a relatively large volume fraction of α-phase (dark region, inset, **Figure 5a**) and a small volume fraction of β-phase (bright region, inset, **Figure 5a**) inside the monolithic TC4 alloy. The average grain size of the primary β-phase is much larger (~250 um) than that of the raw TC4 powders (~86 um, **Figure 9d**), which could be harmful to the mechanical properties of sintered titanium alloys. The microstructure of sintered GNPs/TC4 composites in **Figure 5b** is similar with TC4 alloy except that some TiC and GNPs clusters are located at the grain boundaries. In addition, the residual GNPs are distributed around the cracks, which could provide effective load bearing capability. However, with an increase of the ball milling time, the GNPs/TC4 composite displays a transition from Widmanstätten lamellar microstructures to refined equiaxed microstructures, as compared from **Figures 5a~f.** This transition is beneficial for the enhancement in the strength of composites [35]. As the ball milling time is increased, the highly active carbon atoms possess sufficient mobility and are more likely diffuse into the inner part of Ti matrix to form the discontinuous or continuous TiC structures at a high sintering temperature of 1273 K. This results in the formation of a TiC shell which can effectively constrain the growth

of Ti grains.

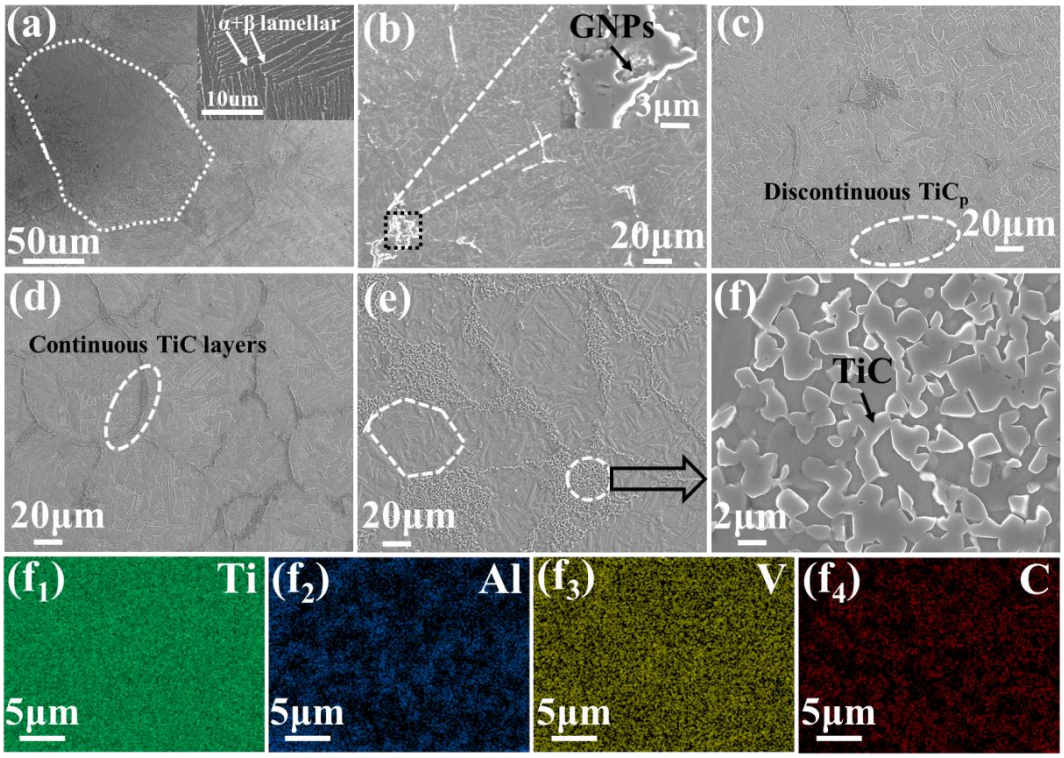

Figure 5. SEM images of as-sintered GNPs/TC4 composites after various milled times (a) 0 hrs, (b) 2 hrs, (c) 5 hrs, (d) 10 hrs, (e) 15 hrs, (f) an enlarged view of marked region in Figure (e) and (f_1)~(f_4) corresponding elements distribution, respectively.

The TEM images of GNPs/TC4 composites with different ball milling times are shown in **Figure 6**. **Figure 6a** shows that the GNPs appear inside the Ti matrix. The interface between the GNPs and Ti matrix is clear and no obvious interfacial reaction products can be identified, which means a short time milling is ineffective to disperse GNPs uniformly. An HRTEM image of GNPs in GNPs/TC4 composites after 2 hrs ball milling is shown in the inset of **Figure 6a**. Its lattice fringe has a spacing of ~ 0.34 nm, corresponding to the interplanar spacing of graphite (0002). However, with

the ball milling times increased to 15 hrs, the grain size of Ti matrix is decreased into the submicron scale as shown in **Figure 6b**. Furthermore, nanoscale reaction products of polygonal TiC particles can be observed to form at the grain boundaries of the Ti matrix, which can be identified by EDS analysis in **Figure 6c** and the selected area electron diffraction (SAED) pattern in **Figure 6d**. There are significant reactions between Ti and C atoms and most of GNPs have been changed into TiC particles owing to the highly cumulative milling energy. The similar phenomenon was also reported in ball-milling of graphene/Al matrix composites [36].

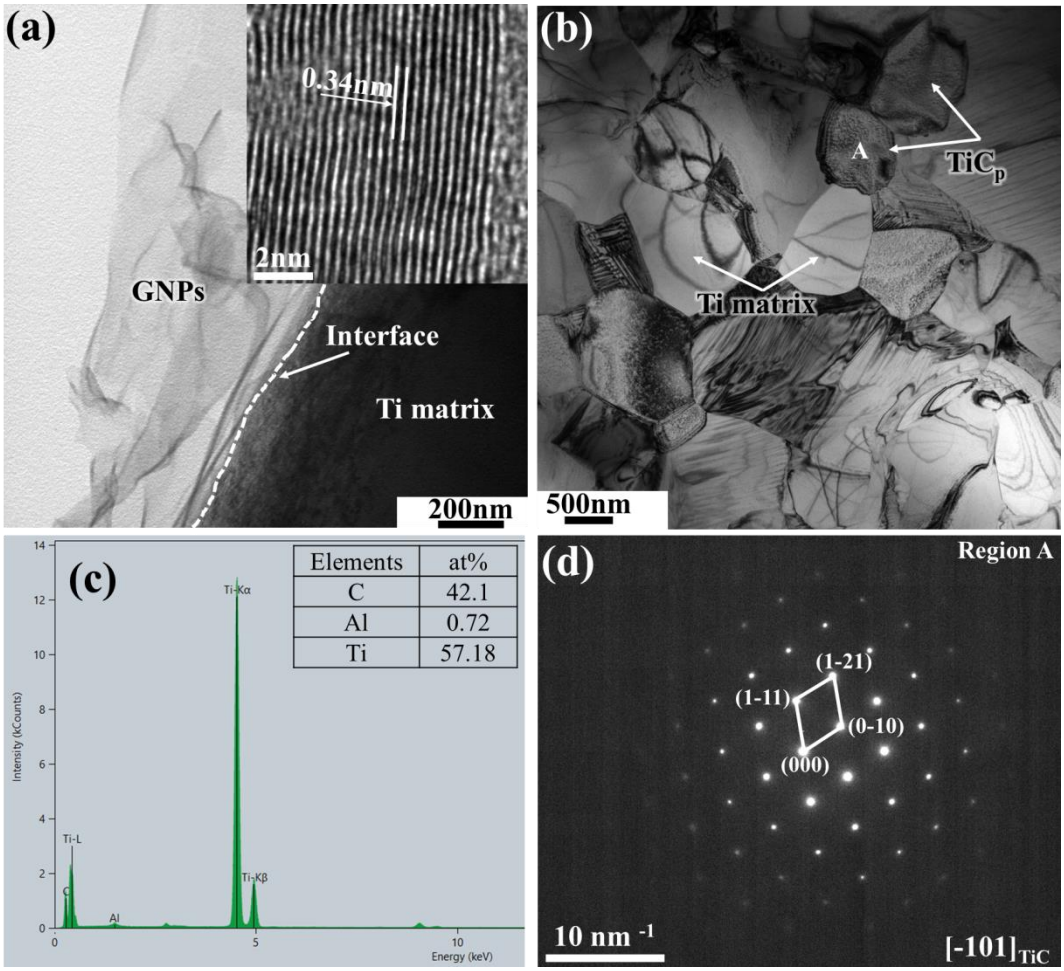

Figure 6. TEM images of sintered GNPs/TC4 composites after ball milling (a) 2 hrs and (b) 15 hrs; (c) EDS analysis and (d) SAED of region A marked in (b), respectively.

The inset in (a) is a HRTEM image of GNPs.

Mechanical properties of the as-sintered TC4 and GNPs/TC4 composites are presented in **Figure 7** and all the results are summarized in **Table 2**. The compressive stress-strain curves of TC4 alloy in **Figure 7a** are consisted of an elastic stage, a plastic yield plateau stage and a parabolic stage. The compressive yield strength of GNPs/TC4 composites is significantly increased compared to that of the monolithic TC4 alloy. The corresponding yield strength and strain at rupture for TC4 alloy was measured as 804.85±10 MPa and 28±0.6%, respectively. The average relative density of the TC4 alloy was 97.46%. However, the compressive yield strength of the C10 and C15 samples are 1.48 GPa and 1.63 GPa, respectively, which have been increased by ~84% and ~103% compared with that of pure TC4 alloys. The average values of relative densities for the C10 and C15 samples were increased to 98.83% and 98.90%, respectively, which are attributed to homogenous formation of an interfacial layer of TiC around GNPs during the HEBM performed at the higher milling energies [37].

The fracture strain of the C2 samples is slightly (30%) higher than that of monolithic TC4 alloy (28%), which is mainly due to the effective load bearing capability of GNPs and the newly formed TiC particles. However, the fracture strain of GNPs/TC4 composites is decreased from 30% to 7% when the ball milling time is increased from 2 hrs to 15 hrs. The sharp decrease in ductility is mainly due to the formation of a continuous network of TiC brittle structures. However, the elastic modulus of composite increases with an increase of ball milling time (**Figure S2**) when the GNPs are introduced into TC4 matrix. The elastic modulus of the C15

samples reaches its highest value of 142.38 GPa, which is an enhancement of 25.86% compared to that of the monolithic TC4 alloy. The increased elastic modulus in composite with the increase of milling time is mainly due to the hard GNPs and *in-situ* formed TiC phases.

The increased strength in graphene or CNTs reinforced metal matrix composites can be attributed to a variety of mechanisms, including grain refinement strengthening [37, 38], load transfer strengthening [16], solution strengthening [27], Orowan looping strengthening, *in-situ* TiC strengthening [39, 40, 41], thermal expansion mismatch strengthening [18]. However, not all these strengthening mechanisms are contributed to the increased strength in the present study. , Microstructures and properties of the Ti matrix composites are strongly dependent on the shape, size and distributional characteristics of reinforcement in the Ti matrix.

First, Orowan looping strengthening mechanism is negligible in this study, because its principle is mainly attributed to the interactions between nano-scale reinforcement particles and the moving dislocations. The reinforcements should be uniformly dispersed in the interior of matrix grains and their sizes should be smaller than 1 mm [42]. However, in this study, the *in-situ* formed TiC particles are all observed at grain boundaries of the Ti matrix and their particle sizes are mostly in micron levels (**Figure 5** and **Figure 6b**).

Second, there exists a small mismatch of coefficient of thermal expansion (CTE) between interfacial products of TiC (~ 7.74×10^{-6}/K), graphene (~ 8×10^{-6}/K [43]) and Ti matrix (~ 10.8×10^{-6}/K). If the composite is slowly cooled down to room

temperature, the dislocations formed at the interfaces due to mismatch can be significantly suppressed at a low cooling rate [44]. Hence, thermal mismatch strengthening is more effective in those fast-quenched composites [45, 46].

Hence, the strengthening mechanism of GNPs/TC4 composites in this study is mainly contributed to a combination of solution strengthening, grain refinement, dislocations strengthening, and load transfer strengthening caused by those *in-situ* formed TiC as well as the remained GNPs.

(1) Grain refinement strengthening shows significant influences to the strength of the composites, because the Ti grain sizes are significantly changed from 253 μm to 83 μm (**Figure 5** and **Figure 7b**). This increased strength ($\Delta\sigma_{gr}$) can be estimated using the Hall-Patch relationship [37]:

$$\Delta\sigma_{gr} = k(d_c^{-0.5} - d_m^{-0.5}) \quad (1)$$

where K is the Halle-Petch coefficient, and usually shows the average effect of the grain boundaries in the polycrystal and is usually 0.68 MPa·m$^{1/2}$ [47], D_c and D_m are the average sizes of TiMCs and monolithic TC4. For the GNPs/TC4 composites, the uniformly distributed GNPs and continuous/discontinuous TiC phases hinder the migration of grain boundary, and thus prevent the growth of Ti grain. Furthermore, the grain refinement is one of the critical factors for the significant increase of hardness (**Figure 7b**).

(2) Interstitial carbon is an effective strengthening element and carbon atoms are preferably confined to α-phase in an α+β titanium alloy. However, further additions of carbon will have minor contribution to the enhancement of strength when the carbon

concentrations are above its limit (e.g., ~0.05 wt% for α-Ti at room temperature [48]). As reported in literature, solid solution strengthening ($\Delta\sigma_{ss}$) induced by carbon interstitial atoms contributes up to 7 MPa per 0.01 wt% carbon [49]. Based on this, the strengthening contribution in 0.2% YS of TiMCs due to carbon additions can be estimated as 35 MPa for all the TC4 composites containing carbon sources above 0.05wt%.

(3) Another key strengthening mechanism is the load transfer strengthening caused by those *in-situ* formed TiC and remained GNPs. According to the previous studies [16, 18, 27, 38, 40], if the strength of TiMCs (σ_c) is regarded as the summation of pure matrix materials strength (σ_m), grain refinement ($\Delta\sigma_{gr}$), solution strengthening ($\Delta\sigma_{ss}$) and load transfer ($\Delta\sigma_{lt}$), then we can obtain $\Delta\sigma_{lt} = \sigma_c - \sigma_m - \Delta\sigma_{ss} - \Delta\sigma_{lt} - \Delta\sigma_{gr}$. In this study a combination of grain refinement strengthening, solid solution strengthening, and load transfer strengthening GNPs and *in-situ* formed TiC has resulted a significant enhancement of mechanical properties for the composites.

The enhancement effect of reinforcements is also attributed to the strong interactions between the reinforcements (TiC and GNPs) and metal matrix. In the GNPs/TC4 composites, the TiC particles are *in-situ* formed, which leads to their strong bonding to the matrix [50]. The crack propagates across the TiC particles, thus resulting in the fracture of these particles, as shown in **Figures 8b** and **c**. This shows that the applied load can be transferred to these TiC particles from matrix. Furthermore, the remained GNPs were pulled out along the direction of compressive

stress (**Figure 8b**) and no obvious voids were observed at the GNPs-Ti interface (**Figure 6a**). These are is in favor of improving the yield strength of the composites through load transfer strengthening of remained GNPs and *in-situ* formed TiC. For the GNPs/Ti composites, the GNPs actively react with titanium matrix during the sintering. However, the formed TiC phases are beneficial to improve Ti-GNPs bonding in the composites due to the formation of strong covalent bonds. In this study, we control the sizes, spatial structure, and discontinuous or continuous structures of TiC phases using both HEBM and SPS processes (see detailed discussion in **supporting information**). The interfacial structures are strongly influenced by ball milling time. Three different types of interfacial structures (e.g., GNPs-Ti, GNPs-TiC and TiC-Ti) are absence in GNPs/TC4 composites [37] after a short ball milling time (see **Figures 5b** and **c**, **Figure 6a**, **Figures 8e** and $\mathbf{e_1}$). However, with an increase of ball milling time, the GNPs are completely reacted with the Ti matrix and form TiC particles or layers (see **Figures 5d** and **e**, **Figure 6b** and **Figures 8h** and $\mathbf{h_1}$). Hence, only TiC-Ti interfaces in GNPs/TC4 composites are still remained after a long time ball milling, thus resulting in degradation of mechanical properties.

The effects of milling time on the average grain size of matrix and the average Vickers hardness of the TC4 alloy and GNPs/TC4 composites are shown in **Figure 7b**. When the ball milling time is increased from 0 to 15 hrs, the grain size of the sintered Ti matrix composites is reduced from ~ 253 μm to ~ 85 μm. This is mainly because the high dislocation density in the ball milled powders during the ball milling process and *in-situ* formed continuous TiC particles around the grain boundary can effectively

prevent the grain growth during the SPS. **Figure 7b** shows that the hardness values of the composites are all higher than that of pure TC4 alloys **(**see **supporting information)**. Whereas the hardness of C2 sample (532.5 HV) is higher than that of C5 sample (507.91 HV) owing to the presence of GNPs (see **Figures 5b** and **6a**) at the grain boundary. The relationships among the size of Ti grains, microhardness, strength and elongation of the GNPs/TC4 composites are summarized into a schematic radar chart as shown in **Figure 7c**. After ball milling for 10 hrs, the GNPs/TC4 composites possess a superior performance, i.e., a high hardness (~539 HV) and compressive yield strength (~1.48 GPa) with a good ductility (~17%). Hence, compared with the results of TC4 matrix composites reported in literature, a good balance of strength and ductility can be achieved by optimal ball milling time of the composite powders based on this study (**Figure 7d**).

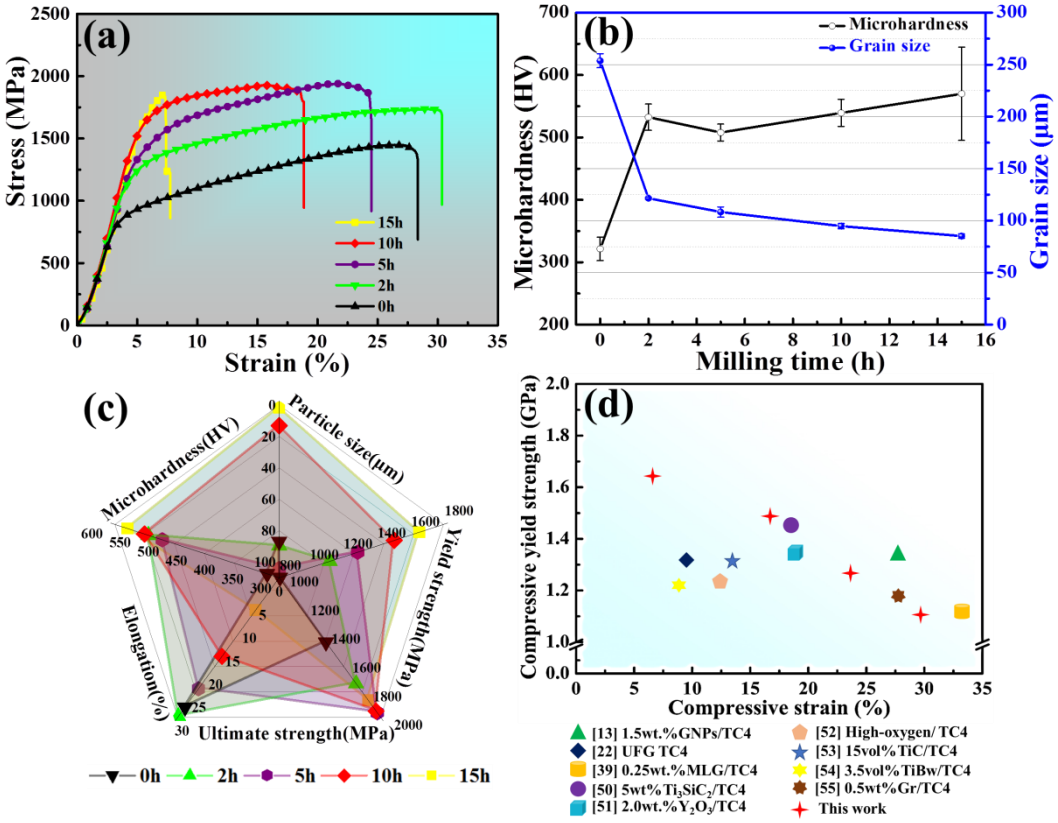

Figure 7. Mechanical properties of pure TC4 and GNPs/TC4 composites. (a) Compressive stress-strain curves. (b) Effect of the milling time on the microhardness and corresponding microstructure. (c) Five factors of radar graph about particle size, compressive yield strength, compressive ultimate strength, elongation and microhardness to reflect the present comprehensive performance. (d) Comparison of the compressive yield strength and strain of TC4 matrix composites in reported articles using ball milling and SPS [13, 22, 39, 50-55], respectively.

Table 2. Mechanical properties of pure TC4 and GNPs/TC4 composites.

Ball milling time (h)	Compressive yield strength (MPa)	Ultimate compressive strength (MPa)	Fracture strain (%)	Hardness (HV)	Relative density (%)
0 (C0)	804.85	1449.02	28	321±19	97.46±0.64
2 (C2)	1099.43	1738.31	30	532.49±21	98.00±0.76
5 (C5)	1265.62	1940.56	24	507.±13	98.23±0.55
10 (C10)	1482.63	1929.32	17	539±22	98.83±0.36
15 (C15)	1631.64	1853.68	7	570±75	98.90±0.52

2.4 Fracture behavior of GNPs/TC4 composites

Figure 8 shows the SEM images of fracture surfaces of the sintered samples after compression tests, along with the schematic drawings of fracture mechanism. **Figures 8a~c** are the fracture surfaces of TC4 alloys, and the fracture occurs along the direction of the maximum shear force, e.g., approximately 45° from the loading direction (**Figure 8a**) without formation of micro-cracks. An enlarged view of the surface shown in **Figure 8b** presents the characteristic parabolic dimples, revealing its nature of ductile fracture. However, the fracture behavior is quite different after the addition of GNPs and also with the gradual increase of ball milling time. When the ball milling time is 5 hrs, as shown in **Figure 8d~f**, fracture surfaces show trans-granular facets in TiC particles and GNPs clusters. The pulling out of GNPs (**Figure 8e$_1$**) from the Ti matrix can be clearly observed, which has enhanced the load transfer capability. With further increase of ball milling time to 15 hrs, the fracture surface of GNPs/TC4 composites reveals significantly increased TiC particles as

shown in **Figures 8g~i**. The dominant failure mode is changed to brittle fracture owing to the formation of cracks due to the TiC particles and interfacial debonding during the plastic deformation (**Figure 8h**). The main reason is the incompatibly plastic deformation between the Ti matrix and the TiC network, thus resulting in interfacial failure/ cracking at higher compressive strains.

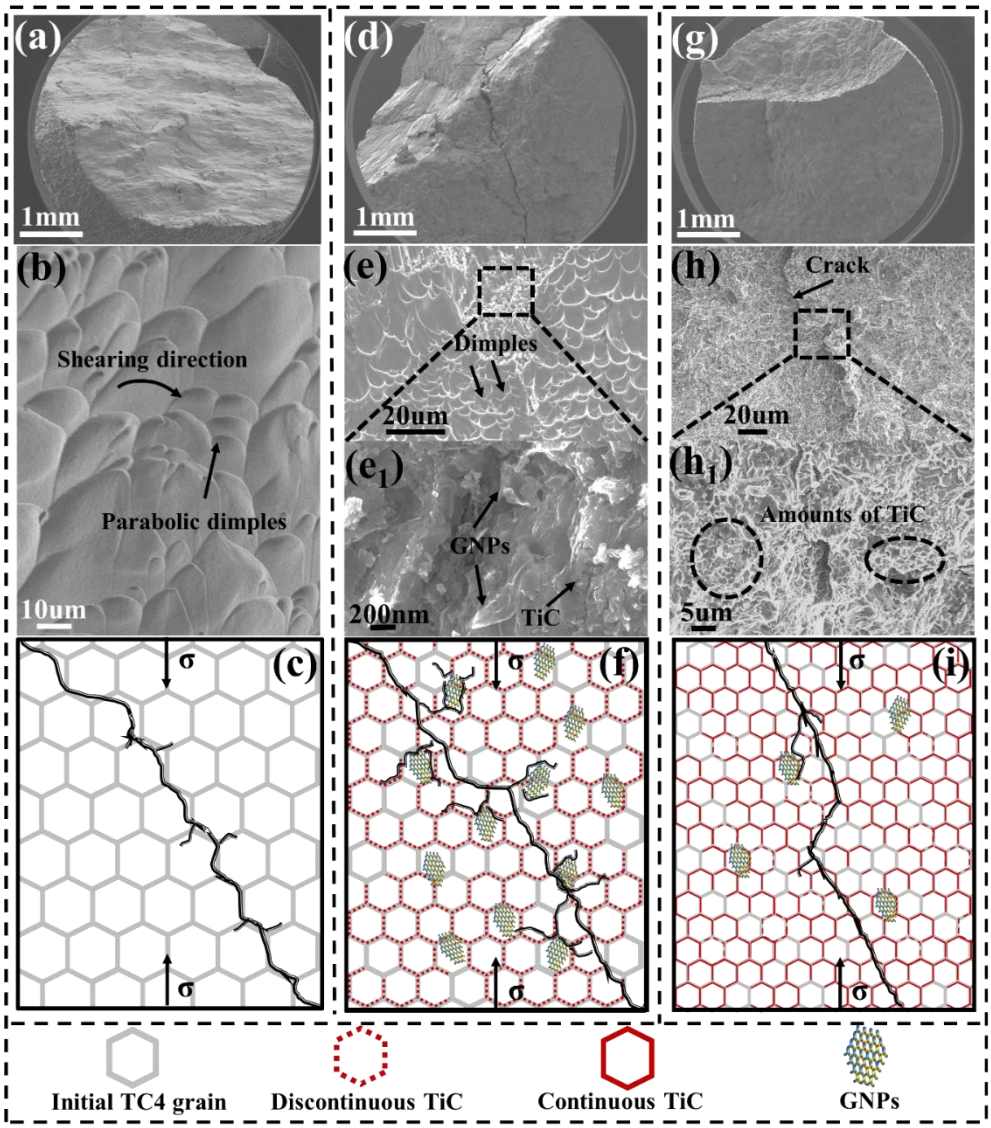

Figure 8. SEM images and high magnifications of compressive fracture for milling time of 0 hrs (a)~(b), 5 hrs (d)~(e), 15 hrs (g)~(h); Corresponding schematic of fracture mechanism in TC4 and GNPs/TC4 composites 0 hrs (c), 5 hrs (f) and 15 hrs

(i), respectively.

3. Conclusions

In this work, the GNPs/TC4 composites prepared with different ball milling times were successfully synthesized using SPS. The effect of ball milling time on the interfacial reactions between GNPs and TC4matrix, microstructures and mechanical properties of the sintered composites were discussed. The main conclusions are as follows:

(1) Ball milling shows significant effects on the GNPs/TC4 mixed powders in two aspects. One is the effectively dispersed GNPs into Ti matrix and the other is the refinement of the grain size of the TC4 powders. However, the TiC nanoparticles were *in-situ* formed and embed onto the surfaces of the TC4 particles when the ball milling time is over 10 hrs.

(2) GNPs/TC4 composites show 36-103% increases in compressive yield strength and 57-78% increases in hardness than those of monolithic TC4 alloy, and the plasticity was reduced with the increase of ball milling time. A good balance between the strength (1.9 GPa) and ductility (17%) of the GNPs/TC4 composites can be well achieved when the ball milling time is 10 hrs.

(3) The improved mechanical properties are mainly attributed to the synergistic strengthening of grain refinement strengthening, solid solution strengthening, load transfer strengthening from the GNPs and *in-situ* formed TiC.

4. Experimental Section

4.1 Raw Materials

Graphene nanoplates (GNPs) were purchased from Nanjing Xian-Feng Nano Materials Technology Co. Ltd., China. Images obtained using TEM (JEOL JEM-2100 Plus) in **Figure 9a** and HRTEM in **Figure 9b** show that the GNPs have large-scale, thin-layered and wrinkled structures. **Figure 9b** also shows that there are many nanoscale defects existed on the edges of GNPs. The image in **Figure 9c** obtained using an atomic force microscope (AFM, Dimension Icon System, Bruker Instruments) shows that the average thickness of GNPs is ~ 2 nm and the length/width ratios are 1~3 μm.

Commercially available Ti-6Al-4V (i.e. TC4) powders with an average size of 86.84±2.36 μm (inset, **Figure 9d**) were purchased from Xi'an Sino-Euro Materials Technologies Co., Ltd., China. They were fabricated using a plasma rotating electrode process and a typical morphology of TC4 spherical powders is shown in **Figure 9d**. **Table 3** lists the characteristics of TC4 powders and GNPs nano-powders.

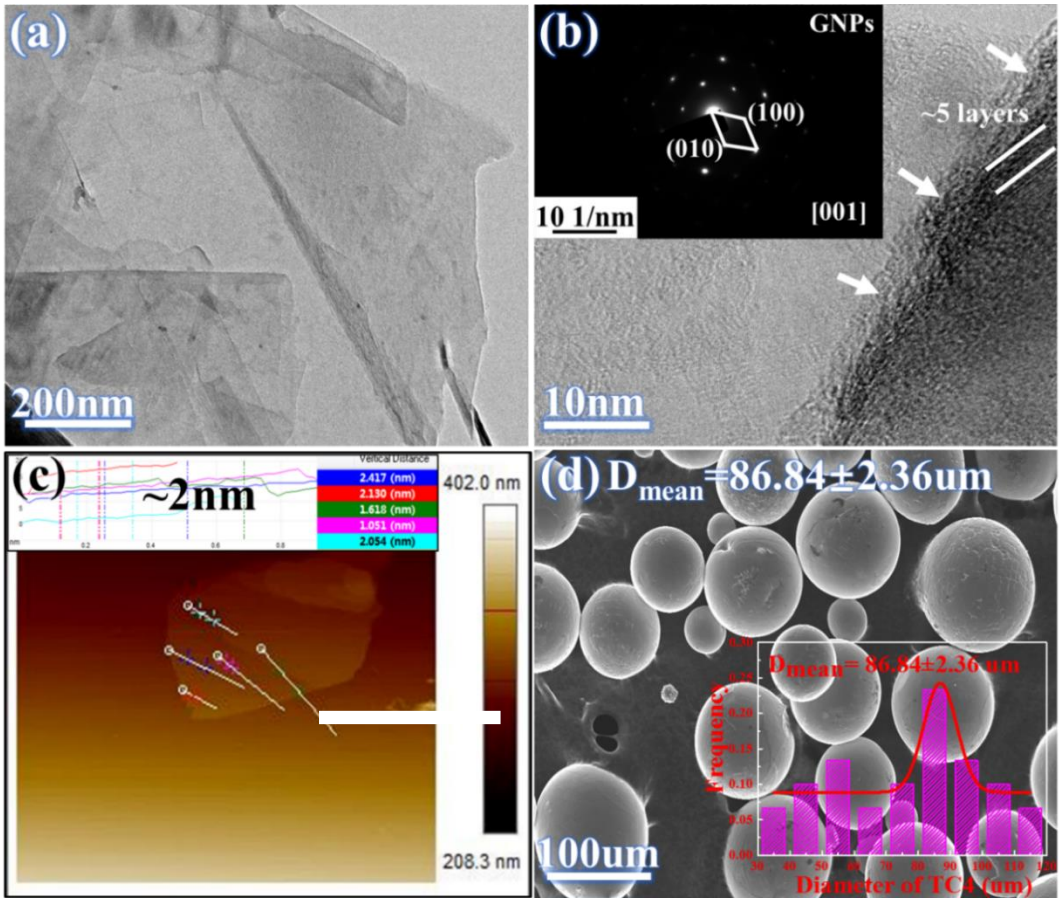

Figure 9. (a) TEM, (b) HRTEM and (c) Top-view AFM image of GNPs and corresponding cross-section height analysis. HRTEM shows less layers structure of the GNPs (< 10 layers) and the nano-scale defects existed on the edges of GNPs. (d) SEM images of the Ti-6Al-4V spherical powders. The inset in 9(d) shows the particle size distribution of TC4 powders.

Table 3. Chemical composition (mass fraction wt%) and characteristics of TC4 and GNPs used in this work.

	Purity (%)	Chemical composition								Particle size (μm)
		Al	V	Fe	C	N	H	O	Ti	
TC4	-	6.17	4.23	0.231	0.008	0.008	0.003	0.12	Bal.	75~150μm
GNPs	> 99	-	-	-	Bal.	0.1	0.05		-	Lateral size 1~3μm Thickness 1~5nm

4.2 Fabrication of GNPs/TC4 Mixtures and Composites

High energy ball milling with ethyl alcohol as a process control agent was employed for dispersion GNPs uniformly into the TC4 powders, and SPS was used to synthesize the composites using these composite powders. The 0.3 g GNPs and 99.7 g TC4 powders were charged into 500 ml stainless steel vials along with WC balls of three sizes (8 mm, 5 mm and 2 mm) in a weight ratio of 5:4:1 and were milled at a speed of 400 rpm for different times (0, 2, 5, 10 and 15 hrs). The ball to powder ratio was maintained at 10:1. In order to avoid oxidation, the HEBM was carried out under a high purity argon protection, and the obtained ball milled powder mixtures were collected within a glove box under an Ar atmosphere. The ball milled mixtures was dried in a vacuum oven at a temperature of 80^{o}C and a dwell time of 24 hrs. After that, the GNPs/TC4 powders were densified using the SPS at 1000 ^{o}C with a time of 5 min and a pressure of 45 MPa. The detailed information about the SPS process has previously been reported in Ref [11].

4.3 Characterization

Microstructural characterization of the mixed powders with different ball milling times was carried out using a field emission scanning electron microscope (FESEM, Zeiss GeminiSEM 500) and the TEM. The phases of the ball-milled composites powders were characterized using the XRD (BrukerAXS D4 Endeavor). Raman spectroscopy was used to investigate structures and defects of GNPs after the ball milling process, and this was performed at room temperature using a Laser Raman Spectrometer (LabRAM HR Evolution) with an excitation wavelength of 532 nm.

XPS (Thermo Fisher ESCALAB Xi^+) was used to evaluate the oxygen containing functional groups and Ti-C bond formation in the composite powders. Samples for AFM imaging were prepared by drop-casting the dispersions of GNPs onto a silicon substrate, which was then allowed to dry in air.

The relative densities of these sintered GNPs/TC4 composites were determined using the Archimedes' method (see **supporting information**), and the obtained results are listed in **Table 2**. Clearly all the composites after various ball milling times show a higher relative density than that of pure TC4 composites. Vickers hardness was tested using an HVS-1000 machine with a load of 300 g and a dwell time of 15 s at five different locations. Then the average value was obtained to represent the hardness of the sample (see **supporting information**). Specimens for compression testing were cut along the direction of pressure loading from the sintered samples with a diameter 4 mm and a height of 8 mm. The compression tests were carried out at room temperature using an MTS810 universal testing machine with a strain rate of 1 mm/min. At least three measurements were performed in order to acquire an average value. Morphologies and compositions of the fractured surfaces were characterized using the SEM.

Associated Content

Notes

The authors declare no competing financial interest.

Acknowledgment

This work was supported by the National Natural Science Foundation of China (No. 51901192), Key Research and Development Projects of Shaanxi Province (No. 2019GY-164), Science and Technology Project of Weiyang District of Xi'an City (No. 201857), as well as Newton Mobility Grant (No. IE161019) through Royal Society and the National Natural Science Foundation of China.

References

[1] Y. Jiao, L.J. Huang, L. Geng, *J. Alloys Compd*, 2018, 767, 1196-1215.

[2] J.W. Lu, Y.Q. Zhao, H.Z. Niu, Y.S. Zhang, Y.Z. Du, W. Zhang, W.T. Huo, *Mater. Sci. Eng., C*, 2016, 62, 36-44.

[3] G. Lutjering, J.C. Williams, Titanium, Second edition ed., springer, 2003.

[4] L.J. Huang, S. Wang, Y.S. Dong, Y.Z. Zhang, F. Pan, L. Geng, H.X. Peng, *Mater. Sci. Eng., A*, 2012, 545, 187-193.

[5] Y. Liu, L.L. Dong, J.W. Lu, W.T. Huo, Y. Du, W. Zhang, Y.S. Zhang, *J. Alloys Compd*, 2020, 819, 152953.

[6] J.W. Lu, Y.Q. Zhao, Y. Du, W. Zhang, Y.S. Zhang, *J. Alloys Compd*, 2019, 778, 115-123.

[7] K. Geng, W.J. Lu, D. Zhang, T. Sakata, H. Mori, *Mater. Des*, 2003, 24, 409-414.

[8] L.G. Wei, X.Y. Liu, Y.Z. Gao, X.W. Lv, N. Hu, M. Chen, *Mater. Des*, 2021, 197, 109261.

[9] L.L. Dong, W.G. Chen, N. Deng, C.H. Zheng, *Chem. Eng. J*, 2016, 306, 754-762.

[10]N. Tian, L.L. Dong, H.L. Wang, Y.Q. Fu, W.T. Huo, Y. Liu, S.J. Yu, Y.S. Zhang, J. Alloy. Compd. doi.org/10.1016/j.jallcom.2021.159093

[11] L.L. Dong, B. Xiao, Y. Liu, Y.L. Li, Y.Q. Fu, Y.Q. Zhao, Y.S. Zhang, *Ceram. Int*, 2018, 44, 17835-17844.

[12] M. Anthony Xavior, H.G. Prashantha Kumar, *Mater. Today*, 2017, 4, 3334-3341.

[13] F.M. Zhang, J. Wang, T.g. Liu, C.Y. Shang, *Mater. Des*, 2020, 186.

[14] Z. Li, Q. Guo, Z.Q. Li, G.L. Fan, D.B. Xiong, Y.S. Su, J. Zhang, D. Zhang, *Nano Lett*, 2015, 15, 8077-8083.

[15] M. Rashad, F.S. Pan, J.Y. Zhang, M. Asif, *J. Alloys Compd*, 2015, 646, 223-232.

[16] X.N. Mu, H.N. Cai, H.M. Zhang, Q.B. Fan, F.C. Wang, Z.H. Zhang, Y.X. Ge, R. Shi, Y. Wu, Z. Wang, D.D. Wang, S. Chang, *Carbon*, 2018, 137, 146-155.

[17] J.S. Zhang, S.F. Yang, Z.X. Chen, Y. Yan, J.W. Zhao, J.S. Li, Z.Y. Jiang, *Ceram. Int*, 2018, 44, 8283-8289.

[18] K. Chu, F. Wang, Y.B. Li, X.H. Wang, D.J. Huang, H. Zhang, *Carbon*, 2018, 133, 127-139.

[19] Y.Y. Jiang, Z.Q. Tan, R. Xu, G.L. Fan, D.B. Xiong, Q. Guo, Y.S. Su, Z.Q. Li, D. Zhang, *Composites Part A*, 2018, 111, 73-82.

[20] X.N. Mu, H.N. Cai, H.M. Zhang, Q.B. Fan, F.C. Wang, X.W. Cheng, Z.H. Zhang, J.B. Li, X.L. Jiao, Y.X. Ge, S. Chang, L. Liu, Y.N. Liu, *Composites Part A*, 2019, 123, 86-96.

[21] T. Yadav, R.M. Yadav, D. Singh, *Nanosci. Nanotechnol*, 2012, 2, 22-48.

[22] Y. Long, H.Y. Zhang, T. Wang, X.L. Huang, Y.Y. Li, J.S. Wu, H.B. Chen, *Mater.*

Sci. Eng., A, 2013, 585, 408-414.

[23] M. Abdellahi, M. Bahmanpour, *Ceram. Int.*, 2015, 41, 1631-1639.

[24] S. Thamer, B.H. A. Tamimi, S.B.H. Farid, *Mater. Today*, 2020, 20, 579-582.

[25] L.L. Dong, W.T. Huo, M. Ahangarkani, B. Zhang, Y.Q. Zhao, Y.S. Zhang, *Mater. Des.*, 2018, 160, 1196-1207.

[26] N. Xiong, R. Bao, J.H. Yi, J.M. Tao, Y.C. Liu, D. Fang, *Mater. Sci. Eng., A*, 2019, 755, 75-84.

[27] L.L. Dong, Y.Q. Fu, Y. Liu, J.W. Lu, W. Zhang, W.T. Huo, L.H. Jin, Y.S. Zhang, *Carbon*, 2021, 173, 41-53.

[28] A.M.K. Esawi, K. Morsi, A. Sayed, M. Taher, S. Lanka, *Compos. Sci. Technol.*, 2010, 70, 2237-2241.

[29] D. Chaira, S. Sangal, B.K. Mishra, *Trans. Indian Inst. Met.*, 2011, 64, 549-554.

[30] K. Vasanthakumar, N.S. Karthiselva, N.M. Chawake, S.R. Bakshi, *J. Alloys Compd.*, 2017, 709, 829-841.

[31] Y. Chen, T. Hwang, M. Marsh, J.S. Williams, *Mater. Sci. Eng., A*, 1997, 226-228, 95-98.

[32] W. Cai, X. Feng, J. Sui, *Rare Met.*, 2012, 31, 48-50.

[33] A. Siokou, F. Ravani, S. Karakalos, O. Frank, M. Kalbac, C. Galiotis, *Appl. Surf. Sci.*, 2011, 257, 9785-9790.

[34] X.H. Gao, Z.M. Guo, Q.F. Geng, P.J. Ma, G. Liu, *Sol. Energy Mater. Sol. Cells*, 2016, 157, 543-549.

[35] L.J. Huang, L. Geng, H.X. Peng, J. Zhang, *Scr. Mater.*, 2011, 64, 844-847.

[36] Z.H. Yu, W.S. Yang, C. Zhou, N.B. Zhang, Z.L. Chao, H. liu, Y.F. Cao, Y. Sun, P.Z. Shao, G.H. Wu, *Carbon*, 2019, 141, 25-39.

[37] L.L. Dong, J.W. Lu, Y.Q. Fu, W.T. Huo, Y. Liu, D.D. Li, Y.S. Zhang, *Carbon*, 2020, 164, 272-286.

[38] K.S. Munir, Y.C. Li, M. Qian, C.E. Wen, *Carbon*, 2016, 99, 384-397.

[39] C.Y. Shang, F.M. Zhang, B. Zhang, F. Chen, *Mater. Des.*, 2020, 196, 109119.

[40] S.F. Li, B. Sun, H. Imai, T. Mimoto, K. Kondoh, *Compos. Part A*, 2013, 48, 57-66.

[41] K. Kondoh, T. Threrujirapapong, J. Umeda, B. Fugetsu, *Compos. Sci. Technol.*, 2012, 72, 1291-1297.

[42] M.L. Wang, D. Chen, Z.X. Chen, Y. Wu, F.F. Wang, N.H. Ma, H.W. Wang, *Mater. Sci. Eng., A*, 2014, 590, 246-254.

[43] D. Yoon, Y.W. Son, H. Cheong, *Nano Lett.*, 2011, 11, 3227-3231.

[44] X. Zhang, C.S. Shi, E.Z. Liu, F. He, L.Y. Ma, Q.Y. Li, J.J. Li, N.Q. Zhao, C.N. He, *Compos. Part A*, 2017, 103, 178-187.

[45] R. George, K.T. Kashyap, R. Rahul, S. Yamdagni, *Scr. Mater.*, 2005, 53, 1159-1163.

[46] S.J. Yoo, S.H. Han, W.J. Kim, *Scr. Mater,*.2013, 68, 711-714.

[47] L.L. Dong, B. Xiao, L.H. Jin, J.W. Lu, Y. Liu, Y.Q. Fu, Y.Q. Zhao, G.H. Wu, Y.S. Zhang, *Ceram. Int.*, 2019, 45, 19370-19379.

[48] M.I. De Barros, D. Rats, L. Vandenbulcke, G. Farges, *Diamond Relat. Mater.*, 1999, 8, 1022-1032.

[49] K.S. Munir, Y. Zheng, D. Zhang, J. Lin, Y. Li, C. Wen, *Mater. Sci. Eng., A*, 2017,

688, 505-523.

[50] X.Y. Huang, Y.M. Gao, Z.P. Wang, Y.L. Yi, Y.R. Wang, *J. Alloys Compd.*, 2019, 792, 907-917.

[51] A. Li, S. Ma, Y. Yang, S. Zhou, L. Shi, M. Liu, *J. Alloys Compd.*, 2018, 768, 49-56.

[52] Y.S. Zhang, J.J. Hu, Y.Q. Zhao, X.F. Bai, W.T. Huo, W. Zhang, L.C. Zhang, *Vacuum*, 2018, 149, 140-145.

[53] S.Y. Liu, Y.C. Shin, *Mater. Des.*, 2017, 136, 185-195.

[54] W.C. Zhang, X.Y. Jiao, Y. Yu, J.L. Yang, Y.J. Feng, *J. Mater. Sci. Technol.*, 2014, 30, 710-714.

[55] A. Li, L. Shi, W. Zhang, S.Q. Zhou, Y.J. Yang, S. Ma, M.B. Liu, Y. Sun, *Mater. Lett.*, 2019, 257, 126750.